Structure, chromium vacancies, and magnetism in a Cr_{12−x}Te_{16} compound

Guixin Cao, Qiang Zhang, Matthias Frontzek, Weiwei Xie, Dongliang Gong, George E. Sterbinsky, and Rongying Jin

Phys. Rev. Materials **3**, 125001 — Published 16 December 2019

DOI: 10.1103/PhysRevMaterials.3.125001

Structure, chromium vacancies, and magnetism in a new $Cr_{12-x}Te_{16}$ compound

Guixin Cao[1,#], Qiang Zhang[1,2,#], Matthias Frontzek[2], Weiwei Xie[3], Dongliang Gong[1], George E. Sterbinsky[4], Rongying Jin[1,*]

[1]Department of Physics and Astronomy, Louisiana State University, Baton Rouge, Louisiana 70803, USA

[2]Neutron Scattering Division, Oak Ridge National Laboratory, Oak Ridge, Tennessee 37831, USA

[3]Department of Chemistry, Louisiana State University, Baton Rouge, LA, 70803, USA
[4]Advanced Photon Source, Argonne National Laboratory, Argonne, IL 60439, USA

Abstract

Binary Cr-Te compounds are known to exhibit various structures and interesting physical properties, which are very sensitive to Cr content and arrangement. We report the structure and physical properties of a new compound $Cr_{12-x}Te_{16}$ with $x \sim 2.65$. $Cr_{9.35}Te_{16}$ crystallizes in the trigonal structure with the space group $P\bar{3}m1$ (No.164), consisting of four different Cr sites (Cr1, Cr2, Cr3, Cr4) with an ordered Cr4 vacant layer. The electrical resistivity, magnetization, specific heat, and neutron diffraction measurements indicate that there is a ferromagnetic transition at $T_{C1} \sim 160$ K with the first-order nature, and an anomaly at $T_{C2} \sim 67$ K. At 5 K, the magnetic moments of Cr2 and Cr3 are aligned along the *c* axis with $2.78\mu_B$/Cr. Detailed neutron diffraction refinement suggests that ordered magnetic moments on Cr1 (fully occupied) and Cr4 (partially occupied) are negligible. The different magnetic response stems from different valence states and different magnetic interactions between Cr2/Cr3 and Cr1/Cr4 as evidenced by the X-ray absorption fine structure measurements. This creates a unique two-dimensional magnetic system with ordered moments confined in the Cr2/Cr3 layer.

# Equal contribution; *Email: rjin@lsu.edu

Binary chromium chalcogenides have aroused considerable interest because they exhibit a large variety of structure, electronic, thermal, and magnetic properties extremely valuable for both fundamental studies and potential applications [1-6]. A characteristic of this material system is that the crystal, magnetic, and electronic structures are very sensitive to the content and ordering of Cr vacancies. For example, stoichiometric CrTe with the NiAs-type structure is unstable at room temperature [7]. However, superstructures derived from the NiAs-type structure can be stabilized at room temperature by reduced Cr concentration, i.e., the Cr : Te ratio being smaller than 1. As the Cr content decreases, there is structural evolution from hexagonal (e.g., Cr_7Te_8) to monoclinic (e.g., Cr_3Te_4), to trigonal (e.g., Cr_2Te_3), to trigonal or monoclinic (e.g., Cr_5Te_8) [7-10]. Correspondingly, the magnetic properties of these compounds vary ranging from ferromagnetic (FM) order with a wide range of Curie temperature (T_C: 150 – 340 K) to canted antiferromagnetic (AFM) order [8-16]. Electronically, these compounds could exhibit metallic, half-metallic, or semiconducting behavior [8-16].

For Cr-Te compounds with reduced Cr content, the created Cr vacancies can be random or ordered [17-19]. For example, Cr_5Te_8 can form the monoclinic structure with ordered Cr vacancies, and the trigonal structure with randomly distributed Cr vacancies [8,17-18]. In Cr_7Te_8, the saturation magnetization varies depending on the arrangement of Cr vacancies [19]. Therefore, it is of great importance to investigate the structure-property relationship in the Cr-Te system. Due to the complexity of Cr distribution, the experimental investigation requires high-quality single-crystalline

samples. In this article, we report the single-crystal growth, crystal structure with information about Cr vacancy arrangement, electronic states, magnetic ordering, electrical and thermodynamic properties of a new compound $Cr_{12-x}Te_{16}$ with $x \sim 2.65$. The relationship between Cr distribution (including vacancy) and physical properties is investigated.

$Cr_{12-x}Te_{16}$ single crystals were grown using the self-flux method. Powder Cr (99.99%, Alfa Aesar) and Te (99.999%, Alfa Aesar) were mixed in the ratio of 1 : 10. After thoroughly grinding, the mixture was sealed in an evacuated quartz tube. The quartz tube was heated up to 1150 °C at the rate of 200 °C/h, held for 24 h, and then slowly cooled at a rate of -2 °C /h. After reaching 900 °C, it was quenched to room temperature. Single crystals are plate-like with well-defined triangular-shaped facets.

For single crystal X-ray diffraction measurements, each single crystal was mounted on the tips of a Kapton loop. Data were collected on a Bruker Apex II X-ray diffractometer with Mo radiation $K\alpha_1$ (λ = 0.71073 Å) over a full sphere of the reciprocal space with 0.5° scans in ω with an exposure time of 10s per frame. The 2θ ranges from 4° to 90°. The SMART software was used for data acquisition. Intensities were extracted and corrected for Lorentz and polarization effects with the SAINT program. Face-indexed numerical absorption corrections were accomplished with XPREP [20]. With the SHELXTL package, the crystal structure was solved using the direct methods and refined by full-matrix least-squares on F^2 [21]. The measurements reveal that our Cr-Te crystals form the trigonal "stuffed" CdI_2-type structure with the space group $P\bar{3}m1$ (No.164) at both room temperature and 100 K. As illustrated in

Figure 1(a), the unit cell, with chemical formula $Cr_{12}Te_{16}$, contains four Cr (Cr1, Cr2, Cr3, Cr4), and four Te (Te1, Te2, Te3, Te4) sites. The refinement indicates that there is ordered Cr vacancy in the Cr4 layer (see Fig. 1(a-b)). According to wavelength-dispersive X-ray spectroscopy (WDS) measurements, the Cr deficiency is $x \sim 2.65$ in $Cr_{12-x}Te_{16}$. Detailed refinement results of $Cr_{9.35}Te_{16}$ are listed in Tables I and II. Note that the Cr ions are each surrounded with six Te atoms (3 above and 3 below the respective Cr ion) forming $CrTe_6$ octahedra as shown in Fig. 1(c). These octahedra are connected via face sharing, resulting in a loop as illustrated in Fig. 1(b). It should be pointed out that $d_{Cr2\text{-}Te1} \sim 2.669$ Å, $d_{Cr2\text{-}Te4} \sim 2.726$ Å, $d_{Cr3\text{-}Te3} \sim 2.7045$ Å, and $d_{Cr3\text{-}Te4} \sim 2.741$ Å. The Cr1 ions however sit equidistant to its surrounding Te4 ions (2.725Å), creating a trigonal prismatic surrounding. The occurrence of octahedral and trigonal prismatic coordination was reported for a series of transition-metal dichalcogenides [22].

Fig. 1(d) shows the three-dimensional Fourier map of observed electron density, revealing the low electron density at the Cr4 site due to its partial occupancy. In addition, X-ray diffraction precession image, displayed in Figure 1(e), shows weak reflections. This indicates the large unit cell with lattice parameters $a = b = 7.8508$ Å and $c = 11.8372$ Å at 100 K, slightly smaller than those at room temperature (see Table I). There are no structural changes between 100 and 300 K. With the ordered vacancy layer (Cr4 layer), we emphasize that our $Cr_{9.35}Te_{16}$ is different from the previously reported Cr-Te compounds [8,18-20]. Especially, it cannot be regarded as the superstructure of Cr_3Te_4. The latter has different crystal structure and physical

properties [7,16,23] than our new compound.

For physical properties measurements, large single crystals with typical size of 4 mm × 4 mm × 1 mm are used. Fig. 2(a) shows the temperature dependence of the in-plane resistivity ρ_{ab} between 2 and 300 K. While it decreases with decreasing temperature, there is a steep change at T_{C1} ~ 160 K, and a kink at T_{C2} ~ 67 K. Near T_{C1}, there is resistivity hysteresis as can be seen in the inset of Fig. 2(a), evident for the first order phase transition. Below T_{C2}, ρ_{ab} exhibits more or less T^2 behavior as demonstrated in Fig. 2(b). The red line is the fit of the resistivity data in the range of 2 - 50 K to $\rho_{ab} = \rho_{ab0} + A_{ab}T^2$, with ρ_{ab0} = 57 μΩ cm and A_{ab} = 2.17 $\times 10^{-2}$ μΩ cm/K^2. This gives the residual resistivity ratio (RRR) ρ(300 K)/ρ_{ab0} ~ 10.9, much higher than that for $Cr_{1-\delta}Te$ [6,16], Cr_2Te_3 [4], or $CrTe_2$ [24]. This suggests the high quality of our single-crystal samples with small residual resistivity. The quadratic temperature dependence of ρ_{ab} indicates dominant electron-electron scattering below 40 K. However, such scattering may be mediated by magnons, if the transitions at T_{C1} and T_{C2} are magnetic in origin. According to theoretical studies [25-27], electronic scattering in weak ferromagnetic metals has also T^2 dependence at low temperatures.

To help understand the nature of two resistivity anomalies, we measure the temperature dependence of the specific heat (C_p), which is shown in Fig. 2(c). Note that there is a spike at T_{C1} and a kink at T_{C2}, confirming the first order phase transition at T_{C1} and likely another transition at T_{C2}. The specific heat spike is enlarged in the inset of Fig. 2(c). At low temperatures, C_p can be described by $\frac{C_p(T)}{T} = \gamma + \beta T^2$. The red line in Fig. 2(d) is the fitting curve with the Sommerfeld coefficients γ = 25.2(6)

mJ mole^{-1} K^{-2} and β = 3.0(2) mJ mole^{-1} K^{-4}. Here, the first term γ measures the electronic contribution while the second term βT^2 decribes the phonon contrbution. According to the Debye model, $\beta = \frac{12\pi^4 RN}{5\theta_D^3}$ (R = 8.314 J/mol-K, and N is the number of atoms in the formula unit). We thus obtain the Debye temperature θ_D ~ 254 K for $Cr_{9.35}Te_{16}$. The good fit of C_p by considering both electron and phonon contributions implies that entropy due to magnons is negligible at low temperatures, if the transitions are originated from magnetic ordering. For our itinerant system, we can also estimate the Kadowaki-Woods (KW) ratio $R_{KW} = A_{ab}/\gamma^2 \sim 3.42\times10^{-5}$ μΩ cm mole^2 K^2 (mJ)$^{-2}$, which suggests strong electron-electron correlation [28].

We now focus on magnetic properties. Figures 3(a) and 3(b) display the temperature dependence of the magnetic susceptibility (χ) taken at zero-field-cooled (ZFC) and field-cooled (FC) modes under the magnetic field of 0.01 T with H // *ab* and H // *c*, respectively. Both χ_{ab} and χ_c show similar behavior above T_{C1} in both ZFC and FC modes. After a sharp rise at T_{C1}, the bifurcation between the ZFC and FC curves becomes pronounced at $T < T_{C1}$. Upon further cooling to $T < T_{C2}$, such bifurcation is even more pronounced. These indicate that anomalies at both T_{C1} and T_{C2} have magnetic origin. Interestingly, the anomaly at T_{C2} is fully suppressed in a field of 1 T, while the magnetic transition at T_{C1} can still be observed as shown in the insets of Figs. 3(a) and 3(b). It should be pointed out that both T_{C1} and T_{C2} are not close to what was observed in Cr_3Te_4 [23]. By fitting χ_{ab} and χ_c in the 240 - 400 K temperature range to the Curie-Weiss law, we obtain the Curie-Weiss temperature □$_{CW}$ = 198 K and the effective magnetic moment $\mu_{eff} \sim 4.08\mu_B$/Cr for H // *ab*, and □$_{CW}$ =

204 K and μ_{eff} ~ 4.12μ_B/Cr for H // *c*, respectively. As plotted in Fig. 3(c) the (red) fitting curves describe experimental χ_{ab} and χ_c well in the selected temperature range. The slight deviation of θ_{CW} and μ_{eff} along two different directions should be attributed to magnetic anisotropy. Note that $\chi_{ab} < \chi_c$, indicating that the magnetic easy axis is along the *c* direction. Nevertheless, the positive θ_{CW} values imply predominant ferromagnetic exchange interaction in $Cr_{9.35}Te_{16}$. Indeed, the *c*-axis magnetization (M_c) at 2 K increases rapidly at low fields, with a tendency to saturate above ~0.5 T as shown in Fig. 3(d)). Such small saturation field implies weak ferromagnetism. The saturation moment for H // *c* is ~23.2μ_B/f.u.. While M_{ab}(H) exhibits similar behavior as M_c(H), it continuously increases with increasing H, reaching 20.7μ_B/f.u. at 7 Tesla. This again indicates that the magnetic easy axis is along the *c* direction.

To unveil magnetism in $Cr_{9.35}Te_{16}$, we performed single-crystal neutron diffraction measurements on both Wide Angle Neutron Diffractometer (WAND) and four-circle single-crystal diffractometer (HB-3A) at Oak Ridge National Laboratory (ORNL). The neutron diffraction patterns on three scattering planes (HK0), (HHL) and (H0L) were collected at WAND at T = 220 K (> T_{C1}) and 5 K (< T_{C2}). Figure 4 shows the representative neutron diffraction pattern in the (HHL) scattering plane for T = 220 K and 5 K. Whereas the diffraction pattern at 220 K only shows the existence of the allowed nuclear peaks by the lattice symmetry $P\bar{3}m1$, the diffraction pattern at 5 K includes both nuclear and magnetic scattering. No pure magnetic peaks emerge, indicating that there is no sign of antiferromagnetic peaks at forbidden $\boldsymbol{Q}$ positions below T_{C2}. Instead, there is an increase of the intensity on a few low-$\boldsymbol{Q}$ nuclear peak

positions, such as (200) and (400) due to contribution from the overlapped magnetic peaks, reflecting ferromagnetic or ferrimagnetic ordering. Interestingly, the intensity of the nuclear peak (100) does not show any detectable change, indicating that the magnetic peak intensity of (100) is much weaker than those of (200) and even (400). This strongly suggests the unusual magnetic structure of $Cr_{9.35}Te_{16}$. In order to determine the magnetic structure, we collected more nuclear and magnetic Bragg peaks in a large-$\boldsymbol{Q}$ region on the same piece of crystal at HB-3A with higher resolution at 220 K and 5 K. The refinement of data at 220 K confirms the trigonal structure with space group $P\bar{3}m1$. Again, no indication for a structural transition is found down to 5 K. Figures 5(a) and 5(b) show the (200) and (20$\bar{2}$) peak intensitiesat at 5 K and 220 K, respectively. The temperature dependence of the integrated intensities for the (200) peak is plotted in Fig. 5(c). The steep increase of the magnetic intensity at T_{C1} is consistent with the first order transition nature as seen in the resistivity, susceptibility, and specific heat. All the magnetic reflections sit on the nuclear peak positions, and can be indexed with the $P\bar{3}m1$ unit cell with a commensurate magnetic propagation vector $\boldsymbol{k}$ = 0. This is again different from that observed in Cr_3Te_4 [23]. There is no increase of the intensities of the (00L) (L = integer) peaks such as (002) or (004). For comparison, Fig. 5(d) shows the unchanged intensity of the (004) peak at 5 K and 220 K, suggesting that (004) has no magnetic contribution. This implies that the magnetic moment points to the *c* axis, since neutron scattering is only sensitive to the magnetic moment that is perpendicular to the scattering vector. SARAH representational analysis program [29] was employed to determine the symmetry of the allowed

magnetic structures. There are six magnetic representations (Γ1, Γ2, Γ3, Γ4, Γ5, Γ6) in total, but only Γ3 and Γ5 are common irreduible representations. However, the integrated intensities of all the nuclear and magnetic reflections can be best fit by employing the Γ3 representation, which yields a ferromagnetic structure with m_c(Cr2) = m_c(Cr3) = 2.76(1)μ_B but negligible magnetic moments at the Cr1 and Cr4 sites. The basis vectors of the allowed magnetic structure for the Γ3 representation are summarized in Table III. Fig. 5(e) displays the refined magnetic structure. Comparison between observed and calculated values of the squared structure factor is shown in Fig. 5(f), where we find a RF factor of 8.39% and χ^2 of 3.32 as the goodness of the fit.

We would like to point out that we have considered various other types of magnetic structures as described below. 1) Any antiferromagnetic models are excluded, since no pure magnetic Bragg peaks were observed. 2) The simple ferromagnetic structure with the same magnetic moment at fully occupied Cr1, Cr2 and Cr3 sites is excluded because such model results in a relatively high magnetic peak intensities of (100) and (101) that have not been observed experimentally. 3) Attempting a ferrimagnetic model with opposite moment direction at Cr1 site relative to the Cr2/Cr3 layer yields m(Cr1) ≈ 0.2μ_B with a much larger error bar of 1.1μ_B, and the refinement quality becomes slightly worse. These indicate that there is negligible ordered moment in the Cr1 layer, which is too weak to be detected via neutron diffraction.

In the following, we disscuss the possible origins of negiligible magnetic moments in Cr1 and Cr4 sites at 5 K as evidenced by neutron diffraction. We recall that Cr_2Te_3, crystallized in a trigonal structure, has a ferromagnetic order with moment of 2.56μ_B at

fully occupied Cr sites but negiligible moment at Cr in the vancancy layer [marked Cr(□)] [14]. This was attributed to weak exchange interaction within the Cr vacancy layer and between neighbouring layers [14]. According to Refs. [14, 23], the interlayer magnetic interaction is extremely sensitive to the *c*-axis Cr-Cr distance with the AFM interaction for distance $d_{Cr\text{-}Cr} < 2.98$ Å but the FM interaction for $d_{Cr\text{-}Cr} > 2.98$ Å. For our $Cr_{9.35}Te_{16}$, the *c*-axis $d_{Cr1\text{-}Cr3} \sim 3.016$ Å at 100 K, right at the transition between AFM and FM exchange interaction [14, 23]. First principles calculations also suggest that the direct Cr-Cr interaction is AFM while indrect Cr-Te-Cr interaction is FM in $CrTe_2$ [30]. The competing AFM and FM interactions lead to weak AFM superimposed on strong FM below the Curie temperature (T_{C1}) [14,15,23,24,30]. The anomaly at T_{C2} of our $Cr_{9.35}Te_{16}$ may have the same origin. Compared to stociotimetric $Cr_{12}Te_{16}$, our $Cr_{9.35}Te_{16}$ has ~88% Cr4 vacancy. The neglegible moment in the Cr4 vacancy layer is well justified, as neither direct nor indirect interactions would play any important role in such a highly-Cr4-vacant layer. Although the Cr1 site is fully occupied, the direct magnetic interaction should be weak, as the distances are 7.85 Å between Cr1-Cr1 within the Cr1 layer and 3.016 Å for Cr1-Cr3 along the *c* axis (discussed above). Possible indirect interactions are via Cr1 – Te – Cr2 and Cr1 – Te – Cr3 (see Fig. 1(b)). Given that the direct interaction between Cr1-Cr3 (see Fig. 1(c)) is at the transition between AFM and FM (discussed above), the indirect interactions are likely weak as well (the direct distance between Cr1 – Cr2 is ~4.905 Å at 100 K). Taking all of these into consideration, Cr1 with neglegible ordered moment can be understood.

In addition to structure consideration, another possibility is that the magnetic moment for each Cr is inherently different due to their different oxidation states. We thus performed the X-ray absorption fine structure spectroscopy (XAFS) at beamline 9-BM of the Advanced Photon Source (APS) using the same single crystal used in the neutron diffraction experiment. The incident X-ray energy was calibrated such that the maximum in the first derivative of the absorption by a reference Cr foil appears at 5989 eV. The X-ray fluorescence from the sample was measured with an energy dispersive silicon drift detector perpendicular to the beam direction and in the plane of the X-ray polarization. The measured Cr Kα signal was normalized by the Te $L_{\alpha,\beta}$ signal, which was measured simultaneously. This ensures that variation in both the incident intensity and effects from sample illumination is corrected. The fluorescence is proportional to the X-ray absorption, except for potential distortion due to self absorption. The measurement is repeated four times for each temperature, and the resulting data is merged using the ATHENA package [31]. Calculations of the pre-edge features in the X-ray absorption near edge structure (XANES) portion of the XAFS were done using the FDMNES program [32]. The input file contains the structural information from Table I and II. The calculated models differ only in the number of *d* electrons. The zero positions of the convoluted spectra are shifted to 5989 eV for comparison with the measured XANES. The output is also multiplied by an arbitrary scaling factor. Fig. 6 shows the XAFS spectra at indicated temperatures. The overall absorption signal is different only in magnitude. Weak changes are within the noise level of the measurement. If a portion of the Cr ions undergoes a valence change, new

peaks would have emerged, and existing ones would have weakened. The model calcuations for the XANES region shown in the inset of Fig. 6 demonstrate that the scenario of all Cr ions having the same valence state (3+) is not in agreement with the experimental data. In fact the best model has a Cr^{3+} state for Cr2 and Cr3 sites and a Cr^{2+} state for the Cr1 and Cr4 sites. A mixture of Cr^{3+} and Cr^{2+} is also found in Cr_2Te_3 [33, 34], in which the Cr *K*-edge XANES is simliar to that measured here in $Cr_{9.35}Te_{16}$.

With Cr2 and Cr3 in the 3+ oxidation state ($3d^3$), the total spin is as high as S = 3/2, corresponding to $gS \approx 3\mu_B$. Considering negligible contribution from Cr1 and Cr4, the expected saturation moment for $Cr_{9.35}Te_{16}$ is $3\mu_B \times 8$ (Cr2+Cr3) = $24\mu_B$, which is in excellent agreement with M_c shown in Fig. 3(d). This indicates that Cr2 and Cr3 are indeed in the high-spin state. However, the effective moment obtained from the Curie-Weiss law fitting of the magnetic susceptibility above T_{C1} is $g\sqrt{S(S+1)} \sim 4.1\mu_B$/Cr, slightly higher than the expected value of $3.87\mu_B$/Cr if assuming S ~3/2 for all Cr ions. It now can be explained by having Cr1 and Cr4 in the high-spin state with S = 2 ($4.9\mu_B$/Cr), yielding an average of $4.02\mu_B$/Cr for $Cr_{9.35}Te_{16}$ above T_{C1}. In order to explain the negligible ordered magnetic moment on the Cr1 and Cr4 sites below the transition temperature T_{C2}, one must assume Cr1(2+) and Cr4(2+) either in the low-spin state with S = 0 or higher-spin state with S ≠ 0 but not ordered. In either case, XAFS spectra remain unchanged since the electron count in the *d* orbitals is the same. While it is not impossible to have the S = 0 state for both Cr1 and Cr4, Hund's rule would require partial occupancy of the t_{2g} orbitals. Thus, it is more likely that Cr1 and/or Cr4 have non-zero moment (i.e., S ≠ 0) but unordered.

In summary, we have synthesized a new compound with chemical formula $Cr_{12-x}Te_{16}$, which contains four Cr and four Te sites. Single crystal x-ray diffraction refinement results in ordered vacancy in the Cr4 layer. This new compound *cannot* be regarded as the superstructure of any known Cr_3Te_4. The electrical resistivity, magnetization, and specific heat measurements indicate that there is a first-order phase transition at $T_{C1} \sim 160$ K, and an anomaly at $T_{C2} \sim 67$ K for $Cr_{9.35}Te_{16}$ ($x \sim 2.65$). While the latter can be suppressed by magnetic field above ~0.5 T, the former remains robust. Single crystal neutron diffraction measurements reveal magnetic peaks at 5 K corresponding solely to ferromagnetic-type magnetic structure. Further data refinement indicates that the observed magnetic moments can be assigned to Cr2 and Cr3, each having $2.76\mu_B$. Remarkably, both Cr1 and Cr4 have negligible magnetic moments, which can be attributed to either the long Cr1-Cr1 and Cr4-Cr4 distances and nearly zero inter-layer exchange interaction with Cr2 and Cr3 below the magnetic transitions. While further investigation is necessary to understand the exact spin state for Cr1 and Cr4, we have built a remarkable Cr-Te system with ordered magnetic moments confined in the Cr2/Cr3 layer.

Acknowledgments

We would like to thank Adam Phelan for initial single crystal X-ray diffraction measurement, and John DiTusa and Jiandi Zhang for fruitful discussion. This material is based upon work supported by the U.S. Department of Energy under EPSCoR Grant No. DE-SC0012432 with additional support from the Louisiana Board of Regents.

Use of the high flux isotope reactor at Oak Ridge National Laboratory was supported by the U.S. Department of Energy (DOE), Office of Basic Energy Sciences, Scientific User Facilities Division. This Research used resources of the Advanced Photon Source, a U.S. DOE Office of Science User Facility operated for the DOE Office of Science by Argonne National Laboratory under Contract No. DE-AC02-06CH11357.

Table I. Single crystal data of $Cr_{9.35}Te_{16}$ at 100(2) K and 300 K. The occupancy on the Cr4 site is a refined parameter yielding a higher Cr content compared to the more reliable WDS value.

Formula	$Cr_{9.35}Te_{16}$	$Cr_{9.35}Te_{16}$
Temperature (K)	100	300
F.W. (g/mol);	1283.92	1283.92
Space group; Z	P-3m1 (No.164);1	P-3m1 (No.164);1
a (Å)	7.8508(3)	7.852(2)
c (Å)	11.8372(5)	11.838(3)
V (Å^3)	631.84(6)	632.1(1)
Absorption Correction	Numerical	Numerical
Extinction Coefficient	0.00055(7)	0.018(3)
θ range (deg)	1.720-45.271	1.720-52.272
No. reflections; R_{int}	18417; 0.0462	19213; 0.0381
No. independent reflections	2002	2542
No. parameters	37	36
R_1; wR_2 (I>2σ(I))	0.0323; 0.0646	0.0545; 0.0838
R_1; wR_2 (all I)	0.0748; 0.0799	0.1168; 0.1402
Goodness of fit	1.030	1.072
Diffraction peak and hole (e$^-$/Å^3)	4.334; –4.402	4.502; –4.953

Table II. Atomic coordinates and equivalent isotropic displacement parameters of $Cr_{9.35}Te_{16}$ at 100(2) K and 300 K. U_{eq} is defined as one-third of the trace of the orthogonalized U_{ij} tensor (Å^2).

Atom	Wyckoff.	Occupancy	x	y	z	U_{eq}
Te1	2d	1	1/3	2/3	0.3834(1)	0.0040(1)
Te2	2d	1	2/3	1/3	0.1317(1)	0.0034(1)
Te3	6i	1	0.1672(1)	0.8328(1)	0.1214(1)	0.0040(1)
Te4	6i	1	0.8323(1)	0.1677(1)	0.3738(1)	0.0040(1)
Cr1	1b	1	0	0	½	0.0015(3)
Cr2	6i	1	0.4927(1)	0.5073(1)	0.2517(1)	0.0040(1)

Cr3	2*c*	1	0	0	0.2452(2)	0.0047(2)
Cr4	3*e*	0.38(1)	0	0.5	0	0.0171(14)

TABLE III. The symmetry-allowed basis vectors (BV) of Γ3 for the space group $P\bar{3}m1$ with $\boldsymbol{k}$ = (0,0,0) in $Cr_{9.35}Te_{16}$. Here are the inequivalent coordinates/atoms for the four Cr sites. 1 for Cr1 site: (0,0,0.5); 6 for Cr2 site: 1. (0.4927, 0.5073, 0.2517), 2. (0.4927, 0.9854, 0.2517), 3. (0.0146, 0.5073, 0.2517), 4. (0.5073, 0.0146, 0.7483), 5. (0.9854, 0.4927, 0.7483), 6. (0.5073, 0.4927, .7483); 2 for Cr3 site: 1. (0, 0, 0.2452), 2. (0, 0, 0.7548); 3 for Cr(4) site: 1. (0, 0.5, 0), 2. (0.5, 0.5, 0), 3. (0.5, 0, 0).

Cr atom	site	*BV*	BV components					
			m//a	m//b	m//c	im//a	im//b	im//c
Cr(1)	ψ_1	1	0	0	12	0	0	0
Cr(2)	ψ_4	1	0	0	2	0	0	0
		2	0	0	2	0	0	0
		3	0	0	2	0	0	0
		4	0	0	2	0	0	0
		5	0	0	2	0	0	0
		6	0	0	2	0	0	0
	ψ_5	1	2	-2	0	0	0	0
		2	2	4	0	0	0	0
		3	-4	-2	0	0	0	0
		4	2	4	0	0	0	0
		5	-4	-2	0	0	0	0
		6	2	-2	0	0	0	0
Cr(3)	ψ_2	1	0	0	6	0	0	0
		2 1	0	0	6	0	0	0
Cr(4)	ψ_2	2	4	2	4	0	0	0
		3	-2	2	4	0	0	0
		1	-2	-4	4	0	0	0
	ψ_3	2	4	2	0	0	0	0
		3	-2	2	0	0	0	0
		1	-2	-4	0	0	0	0
	ψ_4	2	4	2	-8	0	0	0
		3	-2	2	-8	0	0	0
			-2	-4	-8	0	0	0

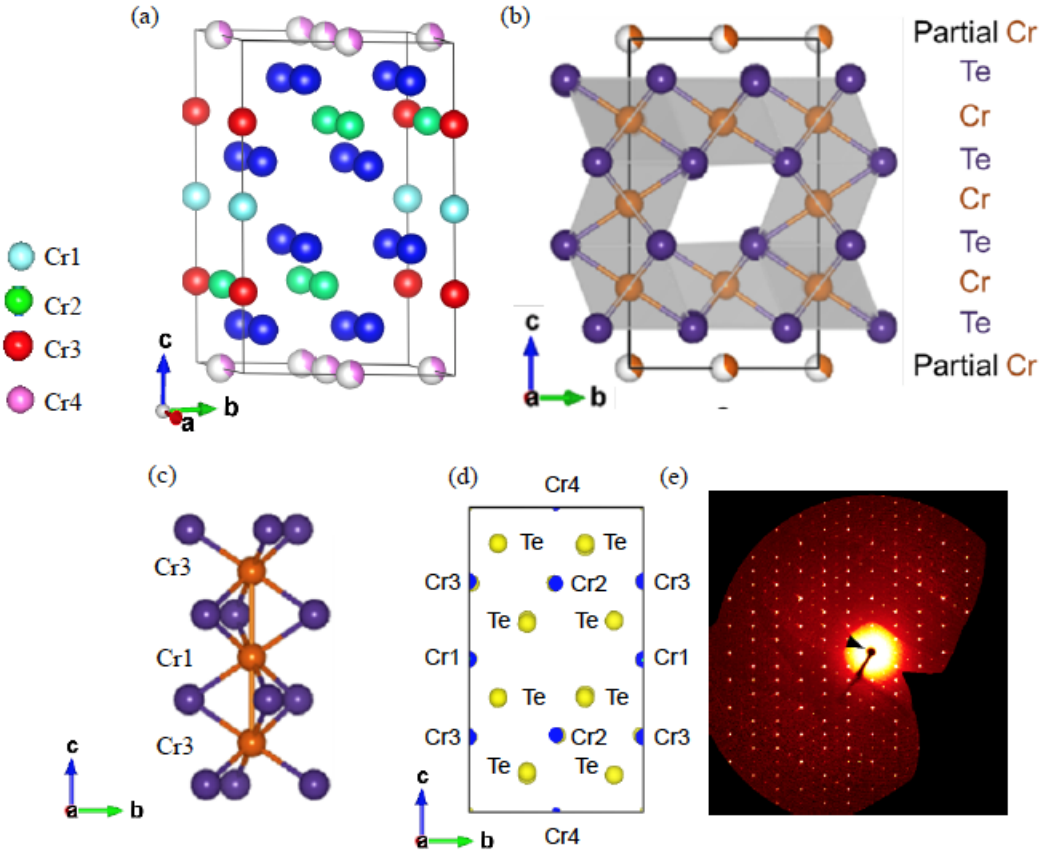

FIG. 1 (color online). (a) Crystal structure of $Cr_{12-x}Te_{16}$ obtained from the refinement of single crystal XRD; (b) Side view of the crystal structure along the *a* direction; (c) Coordination of Cr1 and Cr3 with Te atoms; (d) Fourier map of electron density; (e) X-ray diffraction precession image.

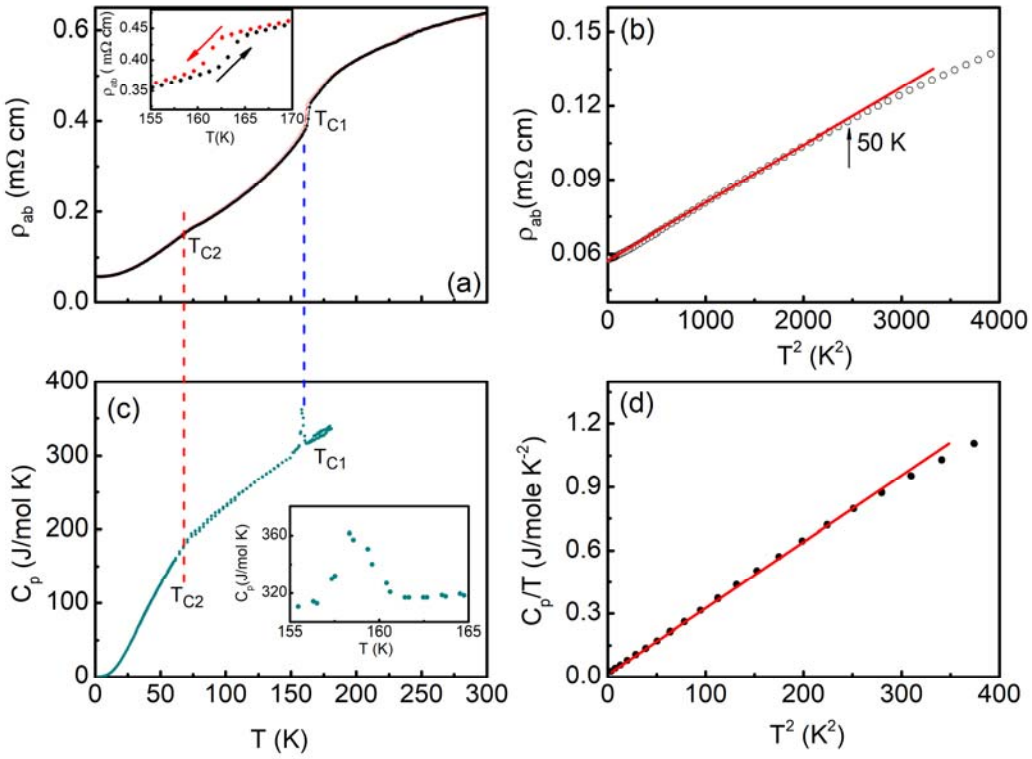

FIG. 2 (color online). (a) Temperature dependence of the *ab*-plane resistivity $\rho_{ab}(T)$ of $Cr_{9.35}Te_{16}$. Inset: $\rho_{ab}(T)$ around T_{C1} in cooling (red) and warming (black) modes; (b) $\rho_{ab}(T)$ plotted as a function of T^2. The solid (red) line is the fit of data to $\rho_{ab} = \rho_{ab0} + A_{ab}T^2$ below 50 K; (c) Temperature dependence of the specific heat C_p. Inset: C_p (T) around T_{C1}; (d) Specific heat plotted as C_p/T vs. T^2. The solid line represents the fit of data to $C_p/T = \gamma + \beta T^2$ between 2 and 15 K.

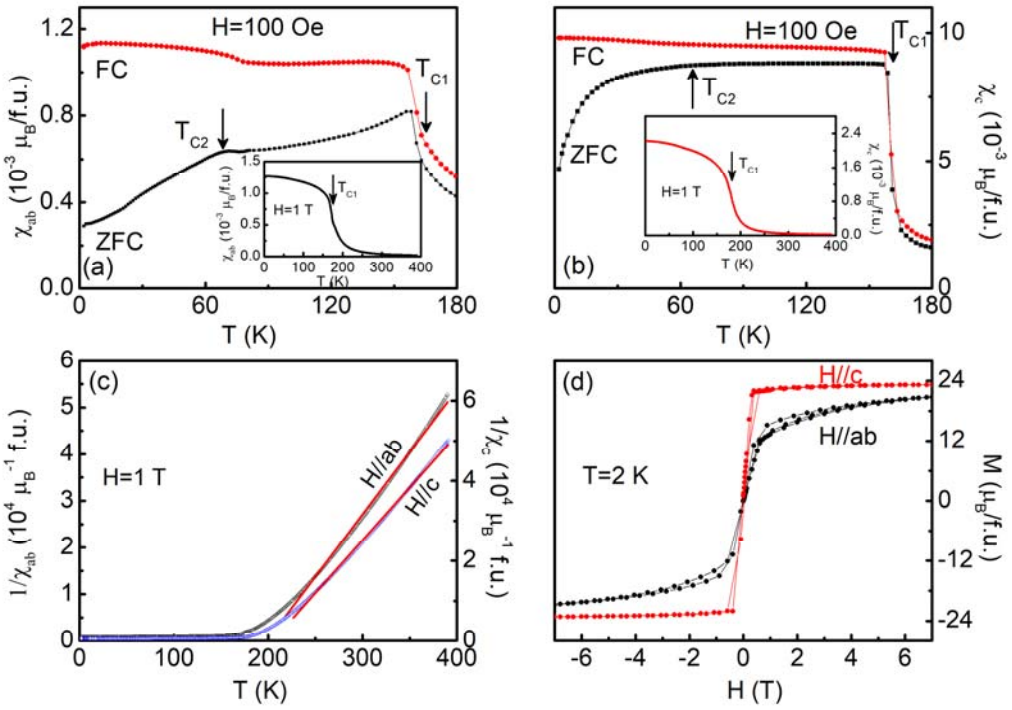

FIG. 3 (color online). Temperature dependence of the susceptibility χ measured under 0.01 T magnetic field in ZFC and FC modes for (a) H // *ab* and (b) H // *c*. Insets of (a) and (b): χ(T) under a field of 1 T for H // *ab* and (b) H // *c*, respectively; (c) Temperature dependence of inverse magnetic susceptibilities. The solid (red) line are the fit of data to the Curie-Weiss law between 250 and 400 K; (d) Magnetic isotherms at 2 K for H // *ab* (black) and H // *c* (red).

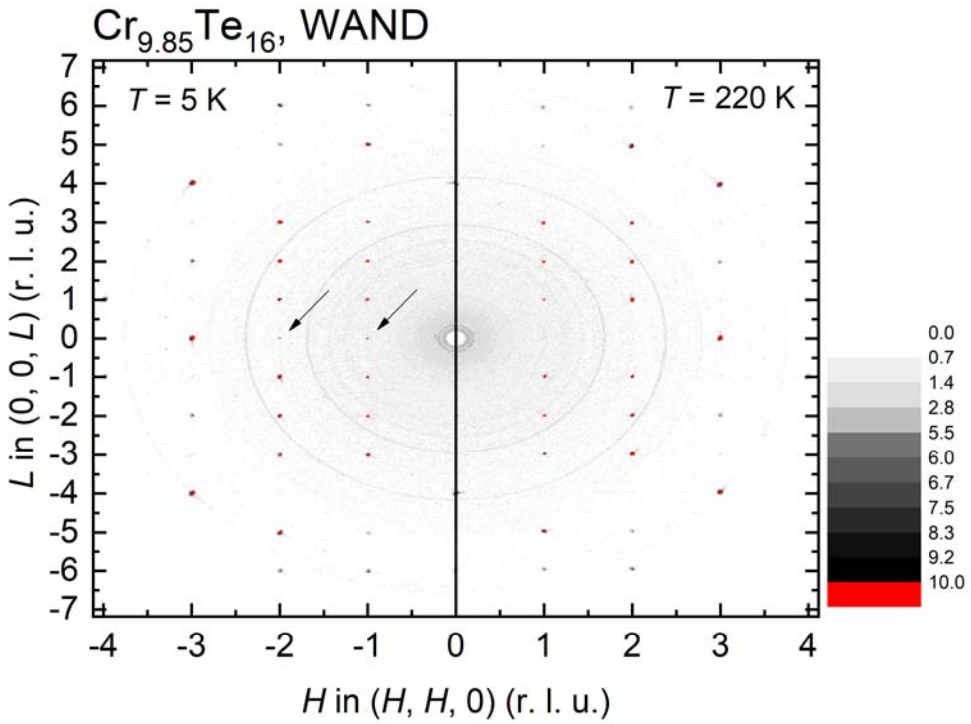

FIG. 4 (color online). Neutron diffraction patterns in the (HHL) scattering plane at T = 5 K (left side) and 220 K (right side), respectively. The contribution from the magnetic peaks on the allowed nuclear peak positions in this plane are marked with arrows.

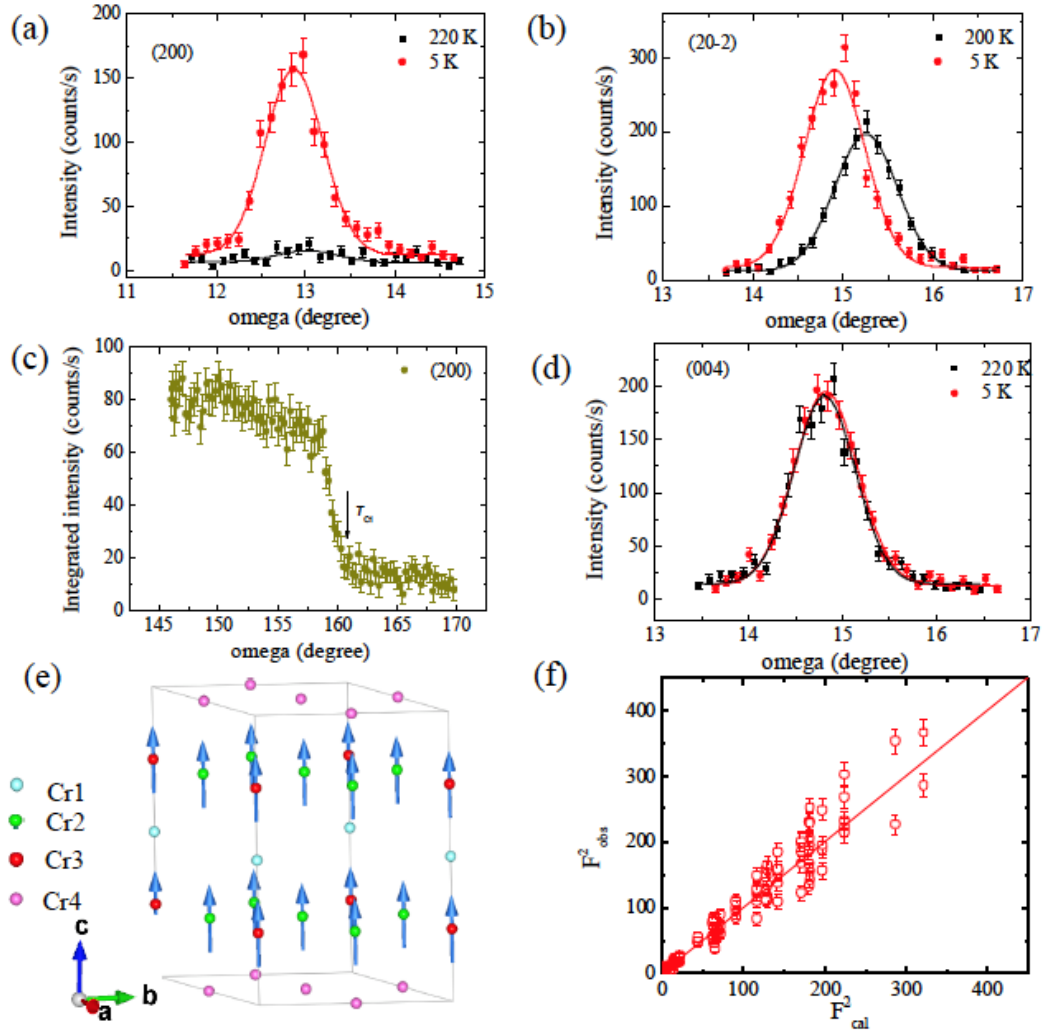

FIG. 5 (color online). (a-b) Rocking curves of the (200) peak (a), and (20-2) peak (b) at 220 and 5 K; (c) Temperature dependence of the integrated intensities for the (200) peak; (d) Rocking curve of the (004) peak at 220 and 5 K; (e) Magnetic structure for $Cr_{9.35}Te_{16}$; (f) Comparison of the observed and calculated squared structure factors for the Γ3 magnetic configuration at 5 K.

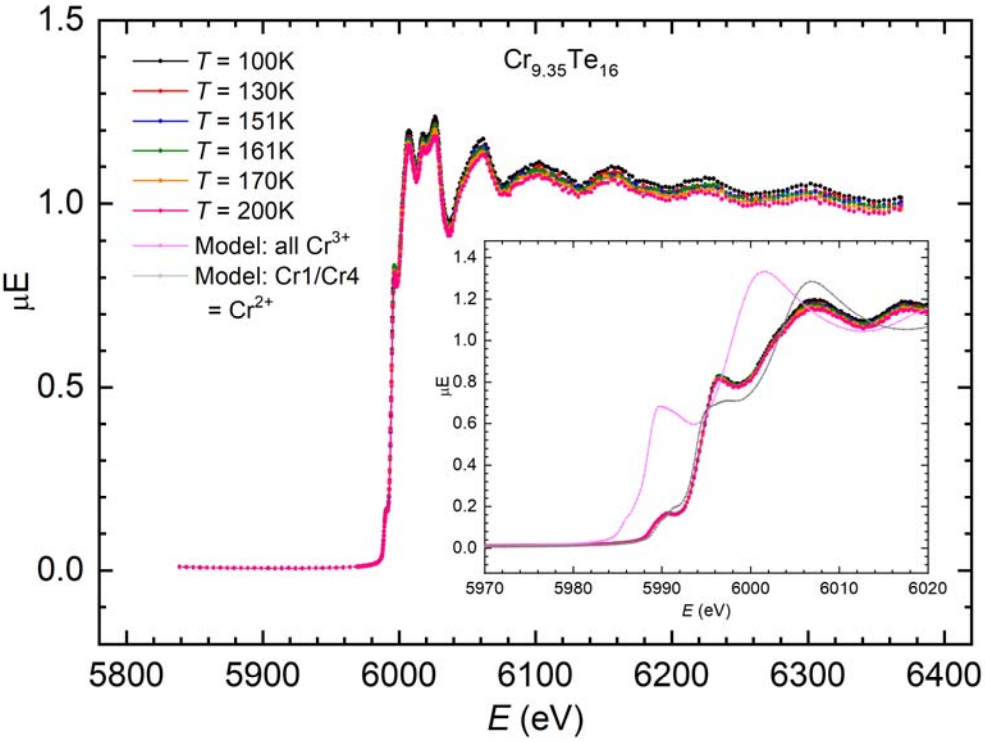

FIG. 6 (color online). XAFS spectra between 100 and 200 K. The inset shows the XANES region with two models: same Cr^{3+} state for all sites (magenta), and combined Cr^{3+} (for Cr2 and Cr3) and Cr^{2+} (for the Cr1 and Cr4) states (grey).

References

[1] M. Chevreton, E. F. Bertaut, F. Jellinek, Acta cryst. **16**, 431 (1963).
[2] K. Sato, Y. Aman, H. Hongu, J. Magn. Magn. Mater. **104**, 1947 (1992).
[3] J. Wontcheu, W. Bensch, S. Mankovsky, S. Polesya, H. Ebert, Prog. Solid State Chem. **37**, 226 (2009).
[4] A. Roy, S. Guchhait, R. Dey, T. Pramanik, C. Hsieh, A. Rai, S. K. Banerjee, ACS Nano **9**, 3772 (2015).
[5] W. Xie, Y. Xu, B. Liu, D. G. Pettifor, Phys. Rev. Lett. **91**, 037204 (2003).
[6] L. Zhou, J. S. Chen, Z. Z. Du, X. S. He, B. C. Ye, G. P. Guo, H. Z. Lu, G. Wang, H. T. He, AIP Adv. **7***,* 125116 (2017).
[7] H. Ipser, K. L. Komarek, K. Klepp, J Less Common Met. **92**, 265 (1983).
[8] Z.-L. Huang, W. Bensch, D. Benea, H. Ebert, J. Solid State Chem. **177,** 3245 (2004).
[9] T. Kanomata, Y. Sugawara, K. Kamishima, H. Mitamura, T. Goto, S. Ohta, *et al.*, J. Magn. Magn. Mater. **177**, 589 (1998).
[10] K. Shimada, T. Saitoh, H. Namatame, A. Fujimori, S. Ishida, S. Asano, M. Matoba, S. Anzai, Phys. Rev. B **53**, 7673 (1996).
[11] K. Lukoschus, S. Kraschinski, C. Näther, W. Bensch, R. Kremer, J. Solid State Chem. **177**, 951 (2004).
[12] H. Haraldsen, A. Neuber, Z. Anorg. Allg. Chem. **234**, 353 (1937).
[13] A. Ohsawa, Y. Yamaguchi, N. Kazama, H. Yamauchi, H. Watanabe, J. Phys. Soc. Jpn. **33**, 1303 (1972).
[14] A. F. Andresen, Acta Chem Scand **24**, 3495 (1970).
[15] Z. –L. Huang, W. Kockelmann, M. Telling, W. Bensch, Solid State Sci. **10**, 1099 (2008).
[16] J. Dijkstra, H. Weitering, C. Van Bruggen, C. Haas, R. De Groot, J. Phys.: Condens. Matter **1**, 9141 (1989).
[17] Z. –L. Huang, W. Bensch, S. Mankovsky, S. Polesya, H. Ebert, R. K. Kremer, J. Solid State Chem. **179**, 2067 (2006).
[18] J. Wontcheu, W. Bensch, S. Mankovsky, S. Polesya, H. Ebert, R. K. Kremer, E. Brucher, J. Solid State Chem. **181**, 1492 (2008).
[19] T. Hashimoto, M. Yamaguchi, J. Phys. Soc. Jpn. **27**, 1121 (1969).
[20] *SHELXTL*, version 6.10, Bruker AXS Inc.: Madison, WI **2000**.
[21] G. M. Sheldrick, Acta Crystallogr. A **64**, 112 (2008).
[22] M. Kertesz, R. Hoffmann, J. Am. Chem. Soc. **106**, 3453 (1984).
[23] E. F. Bertaut, G. Roult, R. Aleonard, R. Pauthenet, M. Chevreton, R. Jansen, *J. Phys. France* **25**, 582 (1964).
[24] D. C. Freitas, R. Weht, A. Sulpice, G. Remeny, P. Strobel, F. Gay, J. Marcus, M. Nunez-Regueiro, J. Phys.: Condens. Matter **27**, 176002 (2015).
[25] K. Ueda and T. Moriya, J. Phys. Soc. Jpn. **39**, 605 (1975).
[26] S. Bharadwaj, D. Belitz, T. R. Kirkpatrick, Phys. Rev. B **89**, 134401 (2014).
[27] T. R. Kirkpatrick, D. Belitz, Phys. Rev. B **97**, 064411 (2018).
[28] A. Jacko, J. Fjærestad, B. Powell, Nat. Phys. **5**, 422 (2009).
[29] A. Wills, Physica B **276,** 680 (2000).
[30] H. Y. Lv, W. J. Lu, D. F. Shao, Y. Liu, Y. P. Sun, Phys. Rev. B **92**, 214419 (2015).

[31] B. Ravel, M. Newville, Journal of Synchrotron Radiation **12**, 537 (2005).
[32] O. Bunau, Y. Joly, J. Phys.: Condens. Matter **21**, 345501 (2009).
[33] L. B. Duffy, A. I. Figueroa, G. van der Laan, T. Hesjedal, Physical Review Materials **1**, 064409 (2017).
[34] H. Ofuchi, N. Ozaki, N. Nishizawa, H. Kinjyo, S. Kuroda, K. Takita, AIP Conference Proceedings **882**, 517 (2007).